Radiating Element Design for Air Traffic Control Radar Systems

P. Rocca, N. Anselmi, M. A. Hannan and A. Massa

Contents

1 Real Radiating Element

As reported in *Fig.*1 the radiating element is composed by two concentric square-ring microstrip, the inner one for S-band radiation and the outer one for L-band radiation. Both of them are fed by a coupling patch as shown in *Fig.*1(a).

Microstrip rings and feeding patches are placed over a substrate of thinckness 1.6 mm and dielectric permittivity of 3.5. The substrate is spaced from the ground plane of a distance t by using a square cavity.

Feeding patches are fed with two coaxial probes connected by SMA connectors on the bottom side of the ground plane.

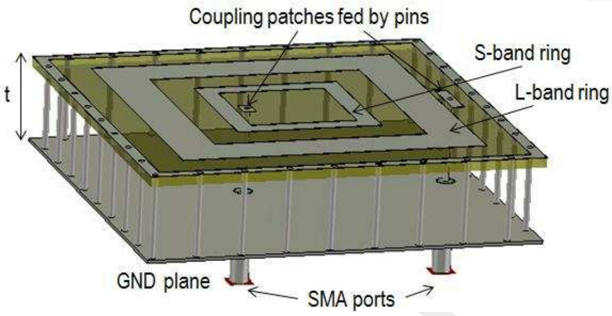

(a)

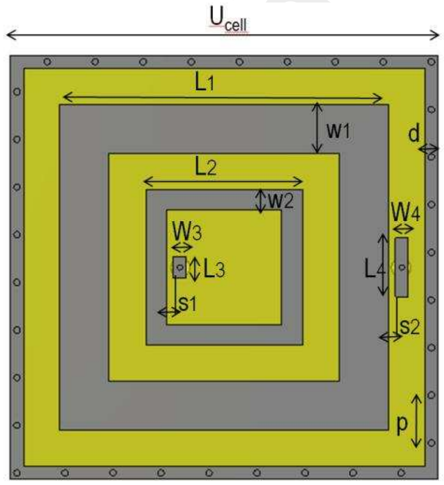

(b)

Figure 1: Radiating element, 3D view (a), top view (b)

Parameter	*Value* [mm]	*Parameter*	*Value* [mm]
t	12	W_3	2
U_{cell}	65	L_4	9
L_1	50	W_4	2
W_1	7.5	s_1	1
L_2	23.8	s_2	1
W_2	3.15	d	2
L_3	3.4	p	7.5

Table I: Antenna element dimensions

Designing parameters are reported in *Tab.*I.

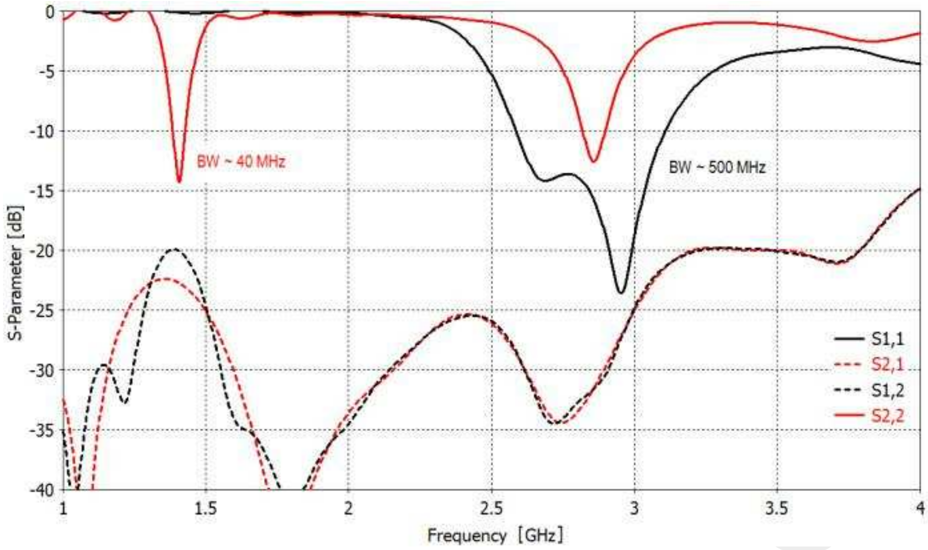

Figure 2: Reflection coefficients for L-band and S-band

In *Fig.*2 are reported the reflection coefficients for the bands L and S. In particular it is noticeable that for S-band the badwidth is about 500 MHz and for L-band is about 40 MHz. It is necessary to divide the square-rings over different layers.

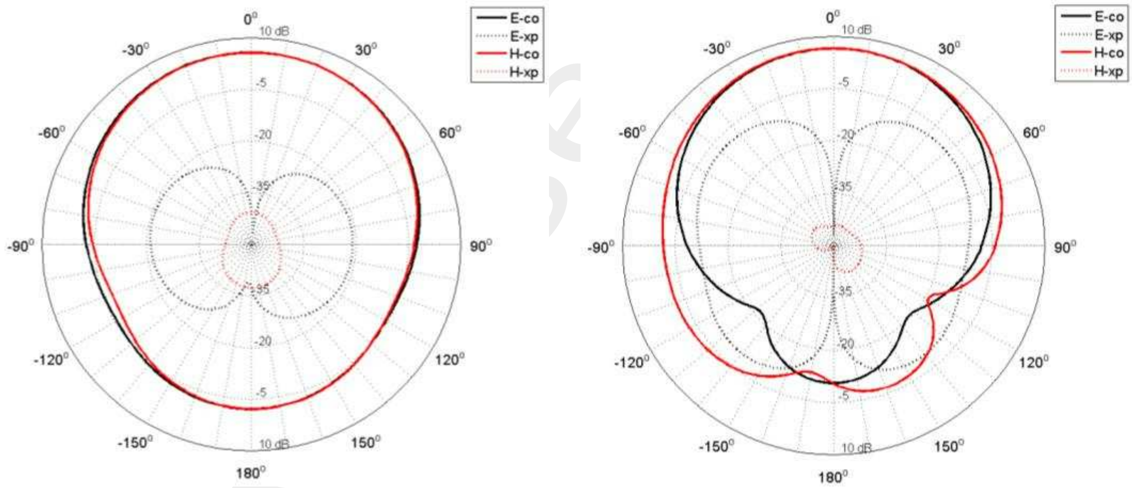

(a) (b)

Figure 3: Power patterns for L-band (a) and S-band (b)

Fig.3 represents power patterns generated by the radiating element, in particular *Fig.3*(a) and *Fig.3*(b) represent the pattern in L-band and S-band respectively.

1.1 Simulated Single Element

The radiating element is shown bellow.

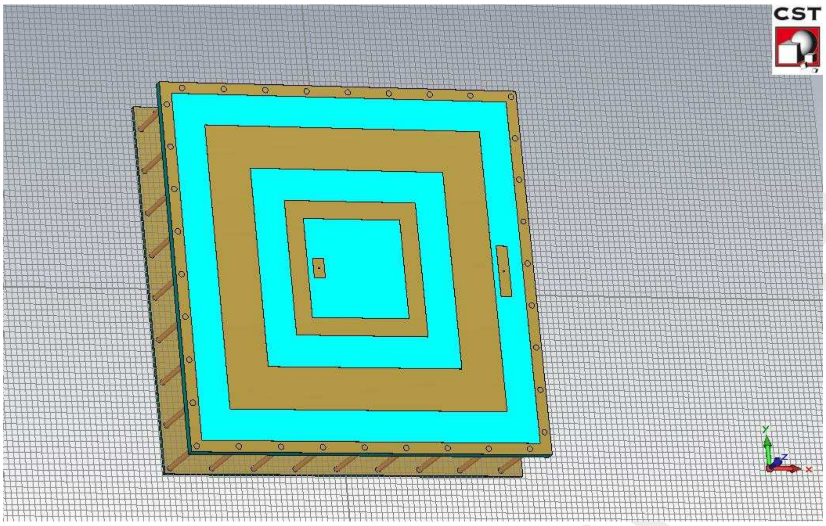

The simulated model respects the geometrical characteristics reported in *Tab.* I. For ground plane substrate the thickness has been set to 0.8 mm.

In figures below are reported simulated element performances. *Fig.*4.*a* and *Fig.*4.*b* represent scattering coefficients on ports 1 and ports 2 respectively. Port 1 feeds the S-band patch (the inner one) and port 2 feeds the L-band patch (the outer one).

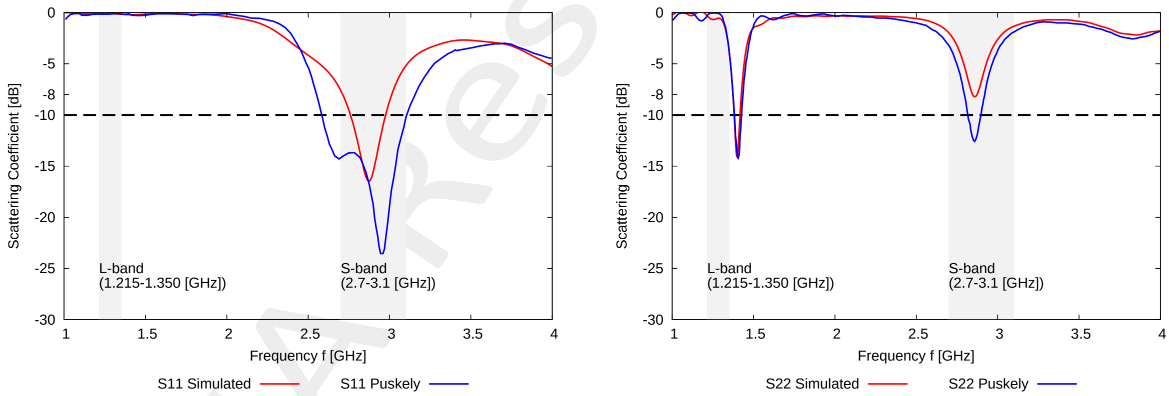

(a) (b)

Figure 4: Scattering coefficients, S11 (a), S22 (b)

It is possible to notice that the scattering coefficients behavior of simulated radiating element is similar but different from the proposed one. In particular the bandwidth in S-band is smaller for both L-band and S-band square-ring radiation.

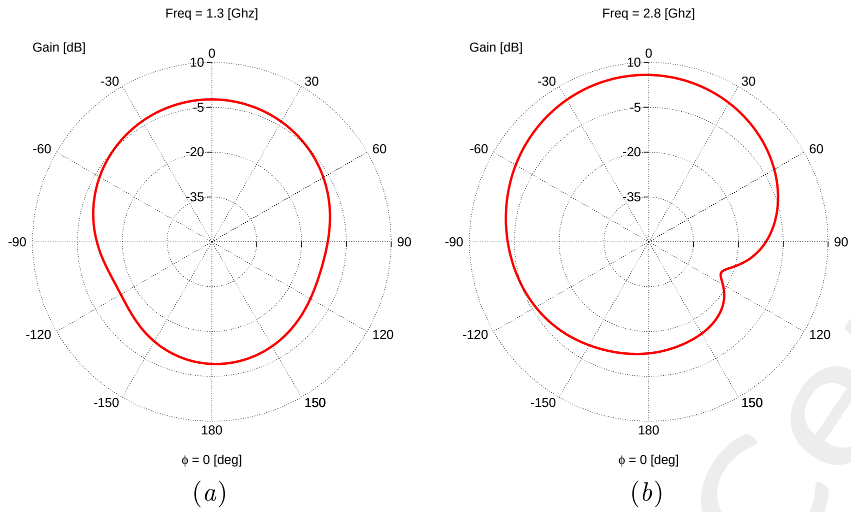

Figure 5: 2D Antenna Gain Pattern for $\phi = 0$[deg]: (a) L-band $f = 1.3$ GHz, (b) S-band $f = 2.8$ GHz

Fig.5.a and *Fig*.5.b show power pattern generated by the simulated model at $f = 1.3$GHz and $f = 2.8$GHz respectively, for $\theta = 0$ and $\phi = 0$.

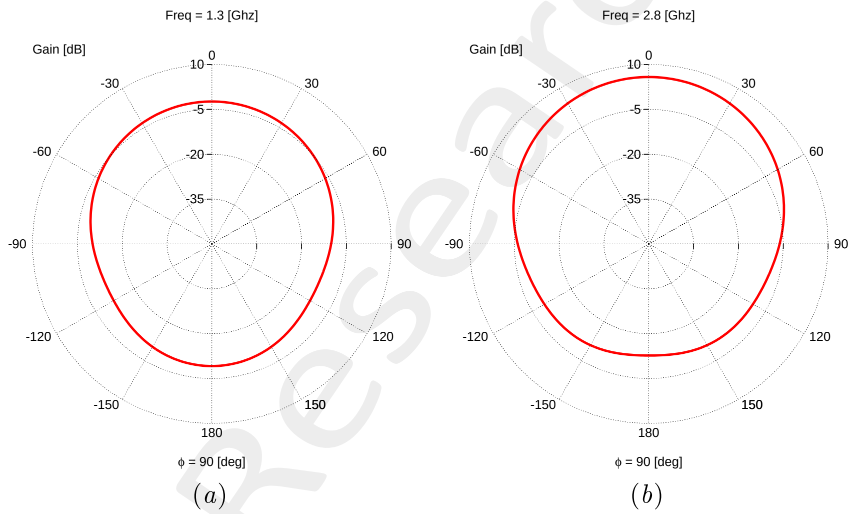

Figure 6: 2D Antenna Gain Pattern for $\phi = 90$[deg]: (a) L-band $f = 1.3$ GHz, (b) S-band $f = 2.8$ GHz

Fig.6.a and *Fig*.6.b show power pattern generated by the simulated model at $f = 1.3$GHz and $f = 2.8$GHz respectively, for $\theta = 0$ and $\phi = 90$.

1.2 Simulated Embedded Element

1.2.1 Model Description

The element previously studied has been used to perform the analysis of the embedded element.

To do that, a geometry composed by five array of five elements each has been taken into account. Array elements has been placed using MT-BCS elements positions of the solution *Best* $M = 16$ at *Section 6.6.1*, in particular considering elements 6, 7, 8, 9, 10.

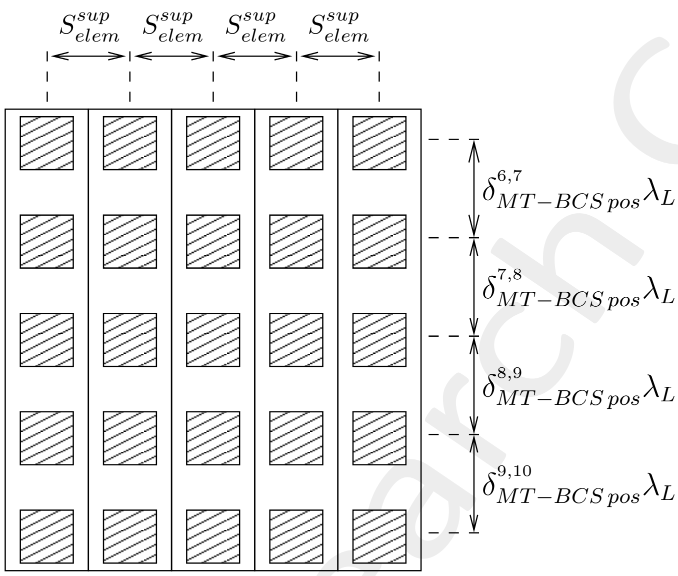

Figure 7: Embedded Element Configuration

Linear arrays are spaced considering the lowest operational frequency band, central frequency of L-band ($1.282\,GHz$), otherwise the elements touch themselves. In *Fig.* 7 is reported the geometry of the considered configuration. In figure above the quantities are defined as follows:

$$\delta_{MT-BCS\,pos}^{i,j} = j_{MT-BCS\,pos}^{th} - i_{MT-BCS\,pos}^{th} \tag{1}$$

$$S_{elem}^{sup} = \frac{2\pi\left[r_{sup} + \Delta_{MT-BCS\,pos}^{1,6}\lambda_L\, sin\,(Tilt)\right]1.8}{360}$$

where

$$r_{sup} = \frac{C}{4\pi}\lambda_L \tag{2}$$

$$\Delta_{MT-BCS\,pos}^{1,6} = \sum_{k=2}^{6}\left(\delta_{MT-BCS\,pos}^{k-1,k}\right). \tag{3}$$

In the above formulation $i_{MT-BCS\,pos}^{th}$, $j_{MT-BCS\,pos}^{th}$ are respectively the positions of the i-th and j-th elements of the MT-BCS linear array obtained from the solution of *Section 6.6.1*, $\delta_{MT-BCS\,pos}^{i,j}$ the distance between them, λ_L the wavelength at $f = 1.282$GHz and S_{elem}^{sup} is the spacing between linear arrays that is grater than $\lambda_L/2$ because we are considering five elements linear arrays composed by the elements 6, 7, 8, 9, 10 of the MT-BCS array of *Section 6.6.1.* r_{sup} is the upper radius of the complete truncated cone geometry with $C = 200$ total number of MT-BCS arrays and $\Delta_{MT-BCS\,pos}^{1,6}$ is the distance between elements 1 and 6 of the *Section 6.6.1* resulting array, useful to compute the distance S_{elem}^{sup}.

Radiating elements respect the geometrical characteristics reported in *Tab.* I. In order to reduce the complexity of the CST model, the substrate supporting the groundplane has been removed.

1.2.2 Model Parameters and Performance

Performance analysis has been performed only considering the L-band part of the radiating elements according to the spacing applied to the five elements linear arrays considered.

In particular the model is characterized by the following geometrical parameters:

- $\delta^{6,7}_{MT-BCS\,pos}\lambda_L = \delta^{7,8}_{MT-BCS\,pos}\lambda_L = \delta^{8,9}_{MT-BCS\,pos}\lambda_L = \delta^{9,10}_{MT-BCS\,pos}\lambda_L = 0.690987\,\lambda_L$
- $\Delta^{1,6}_{MT-BCS\,pos}\lambda_L = 3.469957\lambda_L$
- $r_{sup} = 3724.2257$ mm
- $Tilt = 20$
- $S^{sup}_{elem} = 125.7245$ mm

In figures below are reported simulated embedded element performance. *Fig.*8 represents scattering coefficient on port 1. Port 1 feeds the L-band square ring antenna of the central radiating elements.

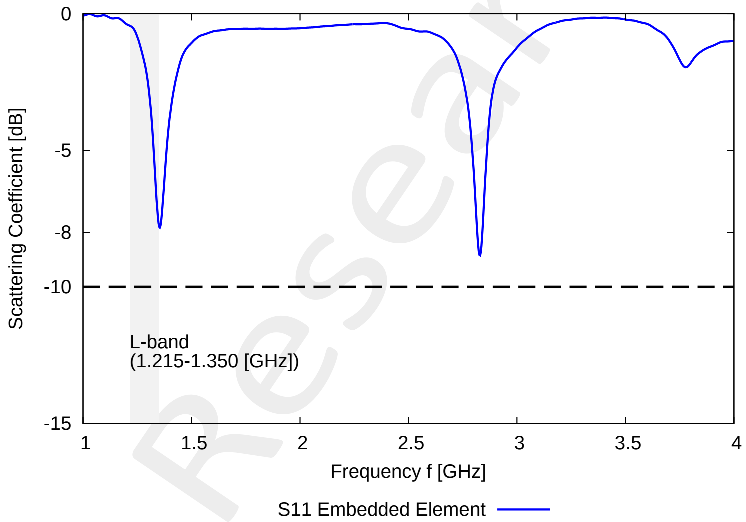

Figure 8: Embedded element scattering coefficients S11

It is noticeable that scattering coefficient does not satisfy the minimum requirement of -10dB and the resonance peak is slightly outside the L-band operational bandwidth. This performance degradation is due to the mutual coupling between radiating elements.

*Fig.*9 shows the radiation diagram at $f = 1.215$ GHz [*Fig.*9.*a*], $f = 1.282$ GHz [*Fig.*9.*b*], $f = 1.350$ GHz [*Fig.*9.*c*]. It is possible to notice that the embedded element radiation pattern exhibits a single and broad main lobe directed towards $\theta = 0$ with quite good characteristics in terms of gain only in the third case at $f = 1.350$ GHz.

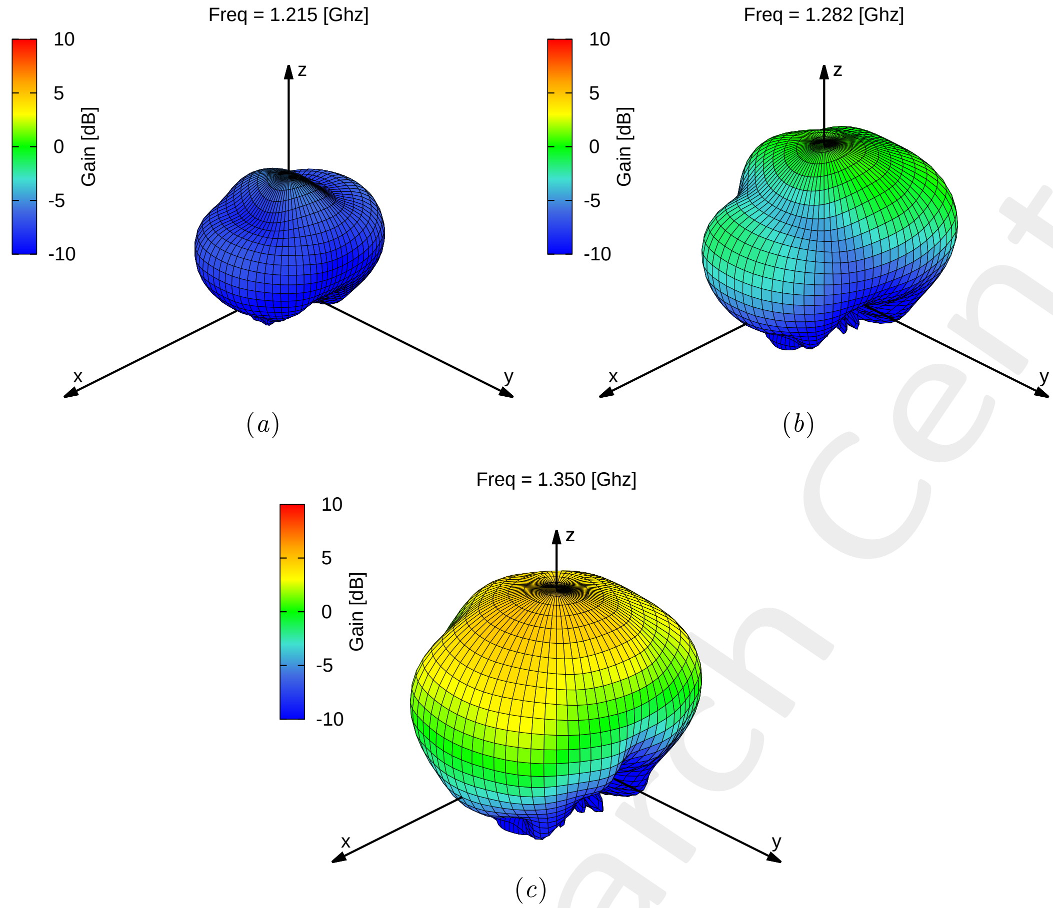

Figure 9: 3D Embedded Element Gain Pattern for: (a) $f = 1.215$ GHz, (b) $f = 1.282$ GHz, (c) $f = 1.350$GHz

Similar consideration can be drawn from the pattern cut in the $\phi = 0$-cut, reported in *Fig.*10. In particular, *Fig.*10 shows the plots of the radiation diagram in the $\phi = 0$ plane at $f = 1.215$GHz *Fig.*10.a, $f = 1.282$ GHz *Fig.*10.b and $f = 1.350$ GHz *Fig.*10.c.

In addition the radiation pattern at $\phi = 90$-cut is reported in *Fig.*11. In particular *Fig.*11 shows the plots of the radiation diagram in the $\phi = 90$ plane at $f = 1.215$GHz *Fig.*11.a, $f = 1.282$ GHz *Fig.*11.b and at $f = 1.350$ GHz *Fig.*11.c.

As expected, the plots in *Fig.*10 and *Fig.*11 confirm that the embedded element radiation pattern is characterized by a single broad main beam with good performance in terms of gain only at $f = 1.350$ GHz.

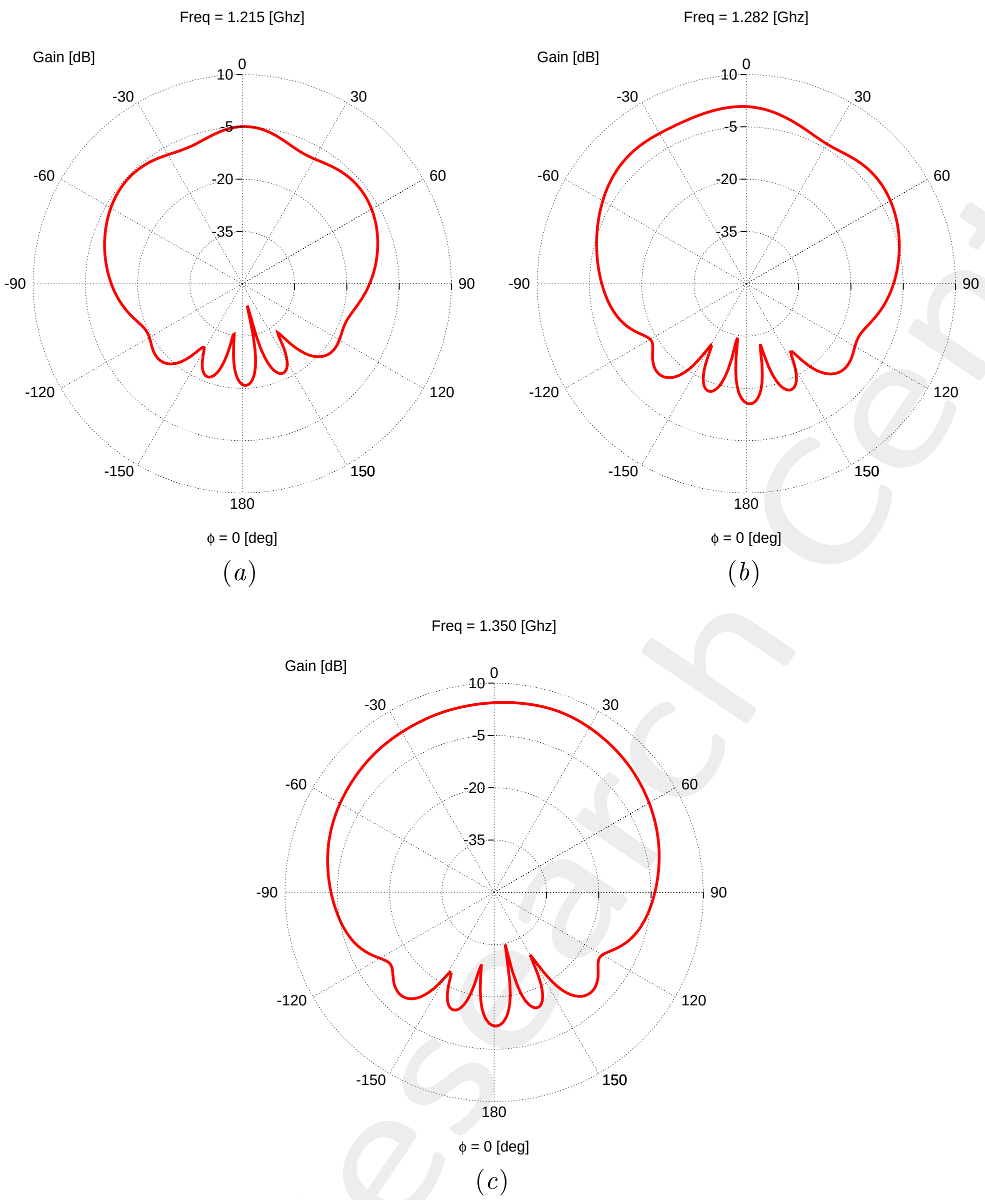

Figure 10: 2D Embedded Element Gain Pattern for $\phi = 0$[deg]: (a) $f = 1.215\,GHz$, (b) $f = 1.282\,GHz$, (c) $f = 1.350\,GHz$

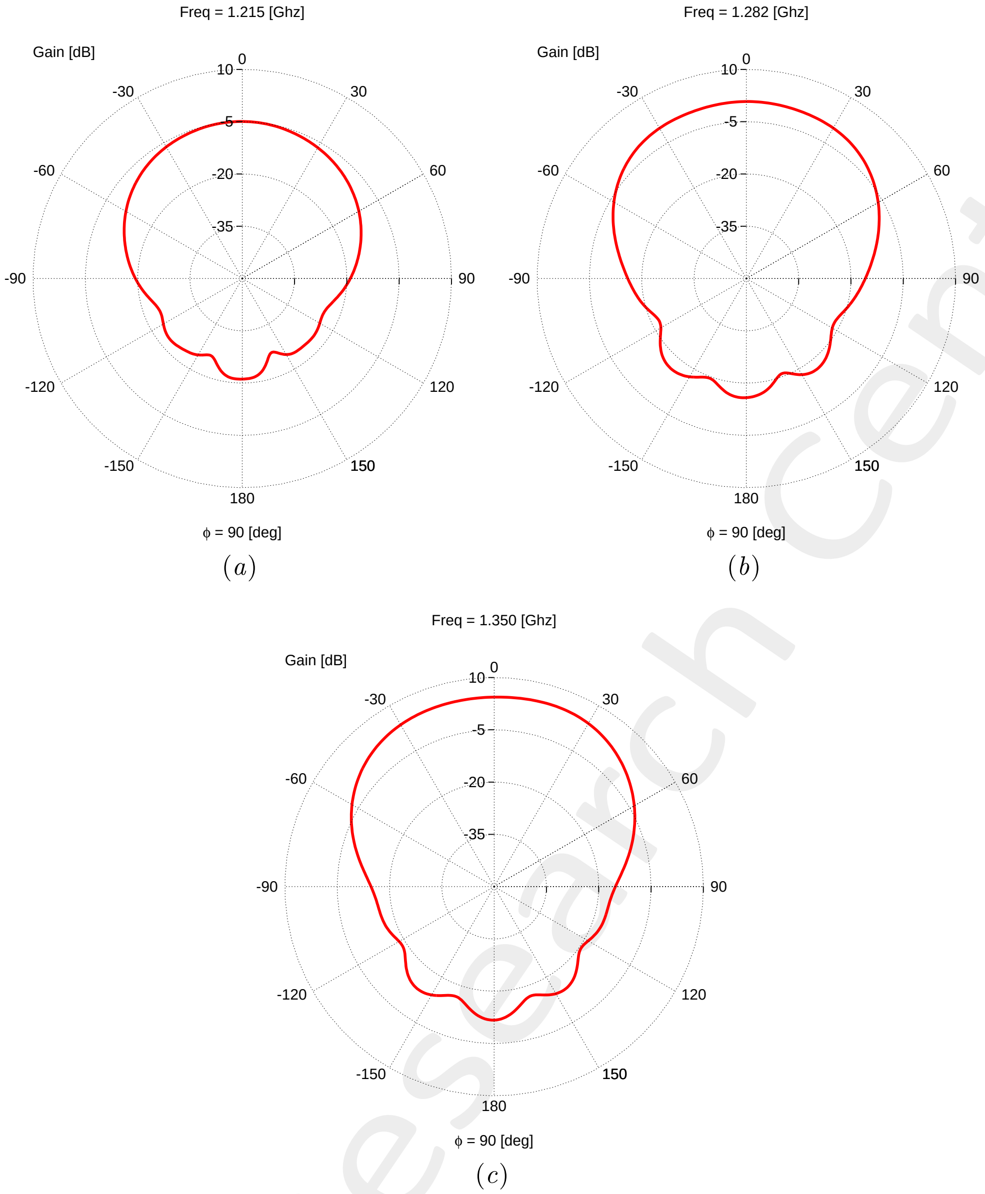

Figure 11: 2D Embedded Element Gain Pattern for $\phi = 90$[deg]: (a) $f = 1.215\,GHz$, (b) $f = 1.282\,GHz$, (c) $f = 1.350\,GHz$

More information on the topics of this document can be found in the following list of references.

References

[1] P. Rocca, G. Oliveri, R. J. Mailloux, and A. Massa, "Unconventional phased array architectures and design Methodologies - A review," *Proceedings of the IEEE - Special Issue on 'Phased Array Technologies'*, Invited Paper, vol. 104, no. 3, pp. 544-560, March 2016.

[2] A. Massa, P. Rocca, and G. Oliveri, "Compressive sensing in electromagnetics - A review," *IEEE Antennas Propag. Mag.*, pp. 224-238, vol. 57, no. 1, Feb. 2015.

[3] F. Zardi, G. Oliveri, M. Salucci, and A. Massa, "Minimum-complexity failure correction in linear arrays via compressive processing," *IEEE Trans. Antennas Propag.*, vol. 69, no. 8, pp. 4504-4516, Aug. 2021.

[4] N. Anselmi, G. Gottardi, G. Oliveri, and A. Massa, "A total-variation sparseness-promoting method for the synthesis of contiguously clustered linear architectures" *IEEE Trans. Antennas Propag.*, vol. 67, no. 7, pp. 4589-4601, Jul. 2019.

[5] M. Salucci, A. Gelmini, G. Oliveri, and A. Massa, "Planar arrays diagnosis by means of an advanced Bayesian compressive processing," *IEEE Tran. Antennas Propag.*, vol. 66, no. 11, pp. 5892-5906, Nov. 2018.

[6] L. Poli, G. Oliveri, P. Rocca, M. Salucci, and A. Massa, "Long-Distance WPT Unconventional Arrays Synthesis" *J. Electromagn. Waves Appl.*, vol. 31, no. 14, pp. 1399-1420, Jul. 2017.

[7] G. Oliveri, M. Salucci, and A. Massa, "Synthesis of modular contiguously clustered linear arrays through a sparseness-regularized solver," *IEEE Trans. Antennas Propag.*, vol. 64, no. 10, pp. 4277-4287, Oct. 2016.

[8] M. Carlin, G. Oliveri, and A. Massa, "Hybrid BCS-deterministic approach for sparse concentric ring isophoric arrays," *IEEE Trans. Antennas Propag.*, vol. 63, no. 1, pp. 378-383, Jan. 2015.

[9] G. Oliveri, E. T. Bekele, F. Robol, and A. Massa, "Sparsening conformal arrays through a versatile BCS-based method," *IEEE Trans. Antennas Propag.*, vol. 62, no. 4, pp. 1681-1689, Apr. 2014.

[10] F. Viani, G. Oliveri, and A. Massa, "Compressive sensing pattern matching techniques for synthesizing planar sparse arrays," *IEEE Trans. Antennas Propag.*, vol. 61, no. 9, pp. 4577-4587, Sept. 2013.

[11] G. Oliveri, P. Rocca, and A. Massa, "Reliable diagnosis of large linear arrays - A Bayesian Compressive Sensing approach," *IEEE Trans. Antennas Propag.*, vol. 60, no. 10, pp. 4627-4636, Oct. 2012.

[12] G. Oliveri, M. Carlin, and A. Massa, "Complex-weight sparse linear array synthesis by Bayesian Compressive Sampling," *IEEE Trans. Antennas Propag.*, vol. 60, no. 5, pp. 2309-2326, May 2012.

[13] G. Oliveri and A. Massa, "Bayesian compressive sampling for pattern synthesis with maximally sparse non-uniform linear arrays," *IEEE Trans. Antennas Propag.*, vol. 59, no. 2, pp. 467-481, Feb. 2011.

[14] A. Benoni, P. Rocca, N. Anselmi, and A. Massa, “Hilbert-ordering based clustering of complex-excitations linear arrays,” *IEEE Trans. Antennas Propag.*, vol. 70, no. 8, pp. 6751-6762, Aug. 2022.

[15] P. Rocca, L. Poli, N. Anselmi, and A. Massa, “Nested optimization for the synthesis of asymmetric shaped beam patterns in sub-arrayed linear antenna arrays,” *IEEE Trans. Antennas Propag.*, vol. 70, no. 5, pp. 3385 - 3397, May 2022.

[16] P. Rocca, L. Poli, A. Polo, and A. Massa, “Optimal excitation matching strategy for sub-arrayed phased linear arrays generating arbitrary shaped beams," *IEEE Trans. Antennas Propag.*, vol. 68, no. 6, pp. 4638-4647, Jun. 2020.

[17] G. Oliveri, G. Gottardi and A. Massa, “A new meta-paradigm for the synthesis of antenna arrays for future wireless communications," *IEEE Trans. Antennas Propag.*, vol. 67, no. 6, pp. 3774-3788, Jun. 2019.

[18] P. Rocca, M. H. Hannan, L. Poli, N. Anselmi, and A. Massa, “Optimal phase-matching strategy for beam scanning of sub-arrayed phased arrays," *IEEE Trans. Antennas Propag.*, vol. 67, no. 2, pp. 951-959, Feb. 2019.

[19] N. Anselmi, P. Rocca, M. Salucci, and A. Massa, “Contiguous phase-clustering in multibeam-on-receive scanning arrays" *IEEE Trans. Antennas Propag.*, vol. 66, no. 11, pp. 5879-5891, Nov. 2018.

[20] L. Poli, G. Oliveri, P. Rocca, M. Salucci, and A. Massa, “Long-distance WPT unconventional arrays synthesis" *J. Electromagn. Waves Appl.*, vol. 31, no. 14, pp. 1399-1420, Jul. 2017.

[21] G. Gottardi, L. Poli, P. Rocca, A. Montanari, A. Aprile, and A. Massa, "Optimal monopulse beamforming for side-looking airborne radars," *IEEE Antennas Wirel. Propag. Lett.*, vol. 16, pp. 1221-1224, 2017.

[22] P. Rocca, M. D’Urso, and L. Poli, “Advanced strategy for large antenna array design with subarray-only amplitude and phase contr," *IEEE Antennas and Wirel. Propag. Lett.*, vol. 13, pp. 91-94, 2014.

[23] L. Manica, P. Rocca, G. Oliveri, and A. Massa, “Synthesis of multi-beam sub-arrayed antennas through an excitation matching strategy," *IEEE Trans. Antennas Propag.*, vol. 59, no. 2, pp. 482-492, Feb. 2011.

[24] M. Salucci, G. Oliveri, and A. Massa, “An innovative inverse source approach for the feasibility-driven design of reflectarrays,” *IEEE Trans. Antennas Propag.*, vol. 70, no. 7, pp. 5468-5480, July 2022.

[25] L. T. P. Bui, N. Anselmi, T. Isernia, P. Rocca, and A. F. Morabito, “On bandwidth maximization of fixed-geometry arrays through convex programming," *J. Electromagn. Waves Appl.*, vol. 34, no. 5, pp. 581-600, 2020.

[26] N. Anselmi, L. Poli, P. Rocca, and A. Massa, “Design of simplified array layouts for preliminary experimental testing and validation of large AESAs," *IEEE Trans. Antennas Propag.*, vol. 66, no. 12, pp. 6906-6920, Dec. 2018.

[27] G. Oliveri and T. Moriyama, “Hybrid PS-CP technique for the synthesis of n-uniform linear arrays with maximum directivity" *J. Electromagn. Waves Appl.*, vol. 29, no. 1, pp. 113-123, Jan. 2015.

[28] P. Rocca and A. Morabito, “Optimal synthesis of reconfigurable planar arrays with simplified architectures for monopulse radar applications" *IEEE Trans. Antennas Propag.*, vol. 63, no. 3, pp. 1048-1058, Mar. 2015.

[29] A. F. Morabito and P. Rocca, “Reducing the number of elements in phase-only reconfigurable arrays generating sum and difference patterns," *IEEE Antennas Wireless Propag. Lett.*, vol. 14, pp. 1338-1341, 2015.

[30] P. Rocca, N. Anselmi, and A. Massa, “Optimal synthesis of robust beamformer weights exploiting interval analysis and convex optimization," *IEEE Trans. Antennas Propag.*, vol. 62, no. 7, pp. 3603-3612, Jul. 2014.

[31] G. Oliveri, G. Gottardi, M. A. Hannan, N. Anselmi, and L. Poli, "Autocorrelation-driven synthesis of antenna arrays - The case of DS-based planar isophoric thinned arrays," *IEEE Trans. Antennas Propag.*, vol. 68, no. 4, pp. 2895-2910, Apr. 2020.

[32] M. Salucci, G. Gottardi, N. Anselmi, and G. Oliveri, “Planar thinned array design by hybrid analytical-stochastic optimization," *IET Microw. Antennas Propag.*, vol. 11, no. 13, pp. 1841-1845, Oct. 2017

[33] T. Moriyama, E. Giarola, M. Salucci, and G. Oliveri, “On the radiation properties of ADS-thinned dipole arrays" *IEICE Electronics Express*, vol. 11, no. 16, pp. 1-10, Aug. 2014.

[34] G. Oliveri, F. Viani, and A. Massa, “Synthesis of linear multi-beam arrays through hierarchical ADS-based interleaving," *IET Microw. Antennas Propag.*, vol. 8, no. 10, pp. 794-808, Jul. 2014.

[35] D. Sartori, G. Oliveri, L. Manica, and A. Massa, “Hybrid Design of non-regular linear arrays with accurate control of the pattern sidelobes," *IEEE Trans. Antennas Propag.*, vol. 61, no. 12, pp. 6237-6242, Dec. 2013.